Journal of the Brazilian Society of Mechanical Sciences and Engineering (2021) 43:278
https://doi.org/10.1007/s40430-021-02999-2

TECHNICAL PAPER

Obtaining flow curve for viscoplastic fluids through inclined open-channel apparatus

Yuri Taglieri Sáo[1] · João Batista Pereira[1] · Guilherme Henrique Fiorot[2] · Geraldo de Freitas Maciel[3]

Received: 8 November 2020 / Accepted: 16 April 2021 / Published online: 30 April 2021
© The Brazilian Society of Mechanical Sciences and Engineering 2021

Abstract

Non-Newtonian fluids are commonly seen in industrial processes, such as those of the oil and mining industry, and in natural flows, like dam ruptures, landslides or mud flows. The hydrodynamic modeling of such processes/phenomena is directly linked to the rheological properties of the flowing fluid, usually characterized through rheometers. The high cost of rheometers and possible inaccessibility for certain applications demand for research of alternative rheometric methods. In order to assess the problem, the present work discusses a detailed experimental methodology to evaluate if the steady and uniform flow in an inclined channel is able to produce the flow curve for the test fluid carbopol 996 gel and work as an alternative rheometer. In order to estimate the shear rates and shear stresses, we measured the normal depth (ultrasonic technique), specific discharge (manual gravimetric method) and free surface velocity (manually and with laser barrier sensors). Based on the theoretical solutions, a simplified fitting procedure was adopted to make possible the assessment of shear rate and shear stress through the experimental data. The obtained flow curves were then compared with the reference flow curve, determined by a commercial R/S rheometer. Results showed that the experimental methods were able to provide the flow curves within acceptable uncertainty and the defined methodology detailed in the work can estimate satisfactorily the flow curve of non-Newtonian fluids. Finally, we highlighted that the wide channel hypothesis is the strongest condition to be guaranteed in order to obtain precise flow curves through the methodology present in this work.

Keywords Flow curve determination · Rheometry · Non-newtonian fluids · Inclined open-channel · Experimental method

1 Introduction

Non-Newtonian fluids are vastly studied in the modeling of natural flows, such as landslides, debris and mud flows, due to the incorporation of sediments, debris and soil into the water [16, 27, 28]. Furthermore, those fluids are also subject of great interest to several applications, including those in the mining, oil, soil science, pharmaceutical and construction industries, among others [4, 17, 23, 25, 31, 42], once the materials commonly used in these areas usually present different behavior and dynamics than those of Newtonian fluids.

In order to understand the flow hydrodynamics specific to each area, these fluids should be characterized regarding their rheological properties (the presence of yield stress, and eventual thixotropic and/or viscoelastic effects, for example). Devices known as rheometers are used to obtain such properties and the material flow curve, since they can impose and measure both the shear stress and the shear rate in a controlled and precise manner. Rheometers, however, are not

Technical Editor: Edson José Soares.

✉ Geraldo de Freitas Maciel
geraldo.f.maciel@unesp.br

Yuri Taglieri Sáo
yuri.sao@unesp.br

João Batista Pereira
jbpereira.eng@gmail.com

Guilherme Henrique Fiorot
guilherme.fiorot@ufrgs.br

[1] Department of Mechanical Engineering, Faculty of Engineering of Ilha Solteira, São Paulo State University, Avenida Brasil, 56, Ilha Solteira, SP 15385-000, Brazil

[2] Mechanical Engineering Department, Engineering College, Federal University of Rio Grande do Sul, Avenida Sarmento Leite, 425, Porto Alegre, RS 90050-170, Brazil

[3] Department of Civil Engineering, Faculty of Engineering of Ilha Solteira, São Paulo State University, Alameda Bahia, 55, Ilha Solteira, SP 15385-000, Brazil

only expensive, but also frequently require the expertise of dedicated operators [35]. In this sense, the search for alternative rheometric characterization of materials is fomented mainly in the academic environments. Such techniques fundamentally reproduce viscometric flows under simple shearing conditions, with previously known and applicable flow characteristics (e. g. stress distribution, velocity profile), whose properties can be easily gauged without a rheometer.

In the context of natural flows and mass movements, rheological properties of materials from debris flow, landslides and mud flows can be obtained through classical rheometry, such as the Vane [34, 39], parallel-plates [8, 39] and coaxial [28] geometries. However, the presence of coarse particles in these flows may invalidate the classical rheometry, since the continuum hypothesis is not respected considering the ratio in rheometer's gap to the grain size [13]. In order to circumvent this impasse, previous works adapted large-scale devices to work as rheometers [13, 40]. Others employed expeditious methods to evaluate the rheological properties of those materials, such as the slump test and inclined plane test [5, 6, 12, 14, 15, 38].

The so-called "alternative techniques" present the same theoretical basis of several rheometers for obtaining flow curves. Thus, the way a capillary rheometer estimates the rheological properties is based on the Hagen–Poiseuille flow; coaxial cylinder and parallel-plate rheometers, though, reproduce a Couette flow. In this sense, it is important to realize that, even if the rheometers are precise and practical to operate, alternative techniques are simple and inexpensive. In other words, the alternative techniques do not stand out due to its exclusiveness, but due to its simplicity and accessibility, which can be sufficient for the rheometric practice in industry and in academic research.

Regarding alternative rheometric techniques, the slump test is a simple, yet robust, fast and inexpensive technique used to estimate the yield stress of a material. A conical or cylindrical mould placed over a smooth surface is filled with the test material and then vertically raised. This procedure allows the material to flow (as a dam-break event), until reaching a final configuration where the yield stress and material's weight are balanced. The difference of height from the initial to the final configuration is used to predict the yield stress of the test material. The yield stress prediction model was firstly idealized by Murata [32] using cementitious materials with the Abrams cone. Later, it was employed in studies with different moulds and materials [3, 38, 41]. More recent studies [36] explored analytical solutions for estimating the yield stress depending on the dominating effects during the slump test, characterizing different flowing regimes (inertial or viscous). These analytical solutions would still be capable to quantify the yield stress of the test fluid. The slump test, however, provides only the yield stress of the material, i.e., a single point of the material's flow curve. Attempts of flow curve determination through the slump test are practically nonexistent in the literature. There are not yet works that explore the shear rates produced during a slump test, therefore preventing the flow curve determination through this method.

Focusing on obtaining the material's entire flow curve, an alternative technique scarcely studied in the literature of non-Newtonian viscoplastic fluids is the steady and uniform flow over an inclined plane. Astarita et al. [2] were pioneers in the area, modeling the analytical formulation of shear rates from the measurement of the flow's specific discharge and normal depth using aqueous glycerol solution, carboxymethyl cellulose (CMC) solutions and bentonite-water mixture. Coleman et al. [10] formulated a function to calculate shear rates based on the free surface velocity in a channel, and on a theoretical explanation of the viscometric flow principles. Ghemmour et al. [24] and Chambon et al. [9] were able to determine the flow curve of carbopol gel and kaolin slurry relating the normal depth and the channel bottom velocity, controlled by a conveyor belt. Coussot and Boyer [12], based on the modeling presented by Astarita et al. [2] and Coleman et al. [10], carried out a series of tests in a rectangular channel, with two mixtures of water and kaolinitic clay, producing a flow curve of the test-fluid in consonance with the results obtained through a Couette geometry rheometer.

Although those works succeeded in predicting the flow curve, new tests must be carried out, using more accurate equipment and based on methodologies that can definitely better validate the inclined channel as a rheometer. In order to contribute to this subject, we performed experimental tests with carbopol gel flowing down an inclined plane and estimated the flow curve using different methods.

Therefore, in pursuance of evaluating alternative non-Newtonian fluid's rheological characterization techniques, the aim of this work is to define and detail an experimental methodology to determine if the steady and uniform flow of a non-Newtonian fluid (carbopol gel) down on an inclined channel is able to provide the flow curve of the fluid. If such premise is met, within in determined tolerance limits, it is likely that centers with no rheometric infrastructure might catch a glimpse of assessing rheological properties in situ, may it be in the context of natural disasters, construction engineering or industrial processes.

In essence, the present work revisits the studies of Astarita et al. [2] and Coleman et al. [10] presenting a linear, detailed and consistent methodology to execute the experiment, to explore and to interpret the results. This work not only uses better performance sensors, but also brings more insight related to the quality of the results obtained by propagating experimental uncertainties to the flow curve. This paper is structured as follows: Sect. 2 presents the mathematical formulation of the flow down an inclined plane for

estimating the shear stress and the shear rate; Sect. 3 details the materials and methodology we used to assess the quantities (discharge, normal depth and free surface velocity) required to employ the mathematical model; Sect. 4 explores the experimental data, uncertainties and confronts the resulting flow curves; lastly, Sect. 5 depicts the final considerations with regard to the presented experiments.

2 Flow down an inclined plane

In this section, we will model the steady and uniform flow down an inclined plane in order to obtain expressions for the shear stress and the shear rate. We will model a wide open channel with predetermined dimensions, through which a free surface test fluid flows in a uniform and steady regime, and whose driving force is the gravitational force. A few hypotheses are established:

- Isothermal flow;
- Fluid with well-defined properties, density ρ and constant rheological parameters, without viscoelastic effects, and whose shear stress τ is a function only of the shear rate $\dot{\gamma}$;
- Viscometric flow;
- No edge and surface tension effects;
- Bidimensional flow, in two directions, x and y, dismissing the third direction z.

Figure 1 shows a scheme of the flow down an inclined plane with θ degrees. The fully-developed velocity field $\vec{V}$ has the non-null component v_x in coordinate x, solely dependent of the coordinate y, hence $\vec{V} = \left(v_x, v_y, v_z\right) = \left(v_x(y), 0, 0\right)$. Equation (1) shows the shear rate tensor $\bar{\bar{D}}$ and Eq. (2) the shear rate $\dot{\gamma}$ as a function of direction y to a given channel slope θ.

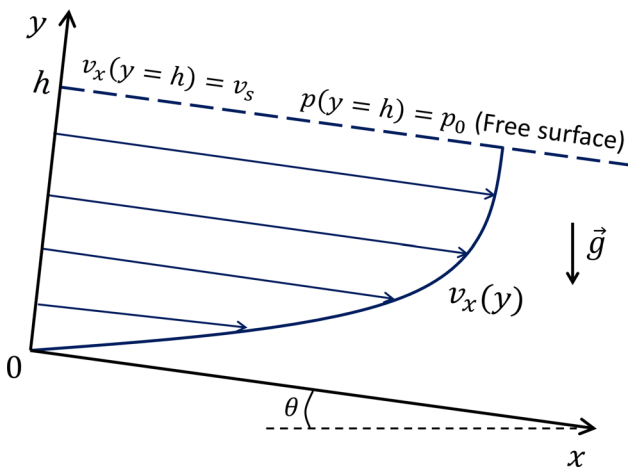

Fig. 1 Scheme of the flow down an inclined plane

$$\bar{\bar{D}} = \begin{bmatrix} 0 & \dot{\gamma} & 0 \\ \dot{\gamma} & 0 & 0 \\ 0 & 0 & 0 \end{bmatrix} \tag{1}$$

$$\dot{\gamma} = \left.\frac{\mathrm{d}v_x}{\mathrm{d}y}\right|_{\theta} \tag{2}$$

According to the hypotheses, we can write the stress tensor $\bar{\bar{\sigma}}$ dependent of $\bar{\bar{S}} = \bar{\bar{S}}(\bar{\bar{D}})$, where $\bar{\bar{S}}$ is the deviatoric part of the stress tensor, function of both the fluid's rheology and the pressure p, as shown in Eq. (3).

$$\bar{\bar{\sigma}} = \bar{\bar{S}} - p\bar{\bar{\delta}} = \begin{bmatrix} 0 & S_{xy} & 0 \\ S_{yx} & 0 & 0 \\ 0 & 0 & 0 \end{bmatrix} - \begin{bmatrix} p & 0 & 0 \\ 0 & p & 0 \\ 0 & 0 & p \end{bmatrix} \tag{3}$$

The shear stress τ can be equaled to the terms of the stress tensor's deviatoric part without loss of generality, with $S_{xy} = S_{yx} = \tau$. In Eq. (4), this generalized tensor is inserted in the equation of balance of momentum, as follows:

$$\rho\frac{D\vec{V}}{Dt} = \rho\vec{g} + \vec{\nabla}\cdot\bar{\bar{\sigma}} \tag{4}$$

where $\vec{g}$ is the gravity acceleration constant and D/Dt denotes the total derivative.

Equation (5) is obtained by integrating the y-component of Eq. (4) from y to the normal depth h and using the x-component of Eq. (4).

$$\frac{\partial}{\partial y}(\rho g y \sin(\theta) + \tau) = \frac{\partial p(x,h)}{\partial x} \tag{5}$$

Since the left side of Eq. (5) is dependent only on coordinate y and the right side only on coordinate x, both sides are equal to a constant C_0. Developing both equations using the following boundary conditions: zero shear stress on the free surface ($\tau(x,h) = 0$); atmospheric pressure on the free surface ($p(x,h) = p_0$); the expression for the shear stress at the bottom τ_b is obtained by Eq. (6):

$$\tau_b = \rho g h \sin(\theta) \tag{6}$$

In order to obtain a function of shear rate based on the specific discharge q, we consider the definition shown in Eq. (7) and perform an integration by parts, along with the no-slip condition in the bottom.

$$q = \int_0^h v_x(y)dy = \int_0^h (h-y)\dot{\gamma}dy \tag{7}$$

We differentiate Eq. (7) in regard to h, knowing that $\dot{\gamma} = f^{-1}(\tau)$, and perform a change of variable $\phi = h - y$ along with Eq. (6), obtaining Eq. (8).

$$f^{-1}(\tau_b) = \dot{\gamma} = \frac{1}{h}\frac{\mathrm{d}q}{\mathrm{d}h}\bigg|_{\theta} \tag{8}$$

A similar development is valid for the free surface velocity v_s, obtaining the shear rate in function of v_s, as shown in Eq. (9).

$$f^{-1}(\tau_b) = \dot{\gamma} = \frac{\mathrm{d}v_s}{\mathrm{d}h}\bigg|_{\theta} \tag{9}$$

As q and v_s vary with h, we can obtain continuous functions $q(h)$ and $v_s(h)$ for each θ in order to apply Eqs. (8) and (9). Along with Eq. (6), we can obtain several points in the rheogram $(\dot{\gamma}, \tau)$, which can be later fitted to the best rheological model available.

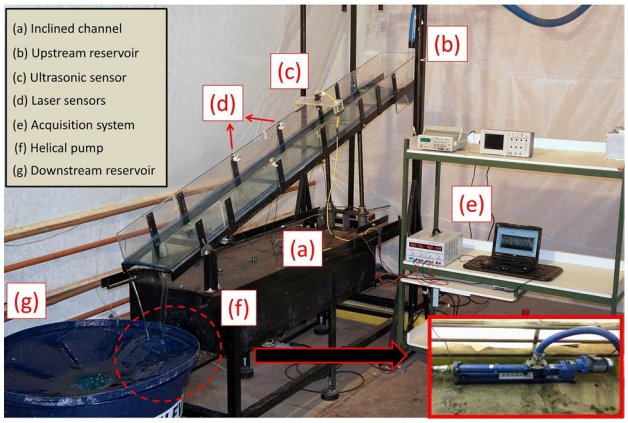

Fig. 2 Inclined open-channel apparatus and detailing of its main components

3 Materials and methods

In order to compose the flow curve through the assessment of the flow properties down an inclined plane, a steady and uniform regime must be maintained, as indicated by the mathematical model in Sect. 2. In the present work, we used the gravimetric method to assess the specific discharge q, the kinematic method to measure the free surface velocity v_s, and the ultrasonic technique to measure the normal flow depth h. The tests were carried out in an experimental apparatus composed of a channel and its accessories, with carbopol gel as the test fluid flowing in a closed circuit. In Subsect. 3.1, we describe the main components of the experimental apparatus and the measurement systems, such as the free surface ultrasonic measurement system and the laser barrier sensors for free surface velocity measurement. In Subsect. 3.2, we present the test fluid carbopol gel 996, define our reference flow curve through an R/S rheometer and estimate the order of magnitude of yield stress using the slump test. Subsection 3.3 outlines the experimental protocol adopted in the tests. Finally, Subsect. 3.4 describes the uncertainties related to the measurements and how they propagate into the flow curve.

3.1 Experimental apparatus

The experimental apparatus employed in the analyses has been used in previous experimental runs and is described in [19] and [29]. The system is composed of an inclined channel, a reservoir, a suction-pump system operating the flow in closed circuit, promoting the test fluid recirculation into the channel. Measurement systems are coupled to the experimental bench to assess desired flow properties. Figure 2 shows the main components of the experimental apparatus.

The rectangular channel of 2.50 m length, 0.15 m height, and 0.30 m width is built with a glass bottom and has acrylic side walls. It is equipped with an upstream reservoir leveled with the channel bottom which receives the test fluid in a uniform regime. In order to reduce significant external vibrations, the channel is fixed over an inertial table designed for isolation of unwanted disturbances. An inclination system was laid out so the channel could operate in variable slopes.

The flow on the channel is carried out by the suction-pump system, composed by a downstream reservoir, a hydraulic pump and the pipeline. The reservoir is constituted by a water tank of 250 L installed downstream from the channel over a wood support. The test fluid stored in it is then suctioned by the helical hydraulic pump (GEREMIA, model WHT32F), especially dimensioned for low discharges of high viscosity fluids. A frequency inverter controls the hydraulic pump's rotation and, consequently, the discharge that is boosted into the channel through the pipeline. The test fluid is finally boosted into the channel's upstream reservoir to descend by gravity once again into the downstream reservoir, completing the closed circuit.

The ultrasonic system used to measure the free surface normal depth does not interfere with the flow properties and dynamics, being considered non-invasive. The ultrasonic transducer (model RPS-401A) operates in the pulse-echo mode, assessing electric tensions linearly proportional to the obstacle's distance (free surface) throughout the time interval between emitted and received ultrasound pulses.

In order to measure the free surface velocity, we used laser barrier sensors, composed of laser beam emitters and receivers installed in the channel's opposing sides, as it can be seen in Fig. 3. The laser beam is continuously emitted in a constant and predetermined power and reaches the receiver in the channel's opposing end, which transforms such intensity into constant electric tension. In the event an obstacle passes between both devices, the laser beam is blocked, the receiver stops detecting it, and the identified electric tension is then modified. This variation in the electric tension marks

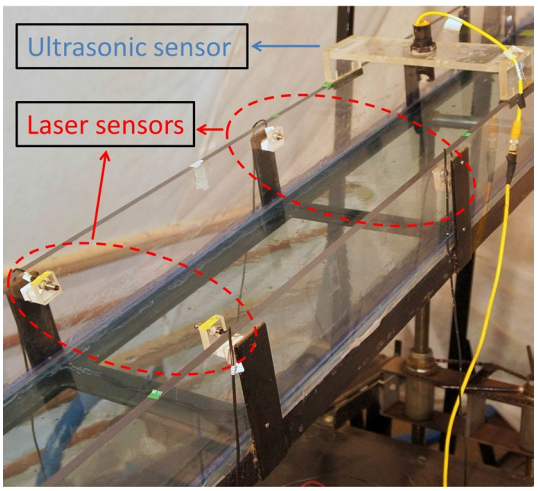

Fig. 3 Positioning of the ultrasonic sensor and laser barrier sensors above the inclined channel

the instant in time the obstacle passes between the embedded emitter–receiver pair. By installing multiple emitter–receiver pairs (separate in predetermined distances) along the channel, we can obtain the necessary time for the flow to go through the given distance, making it possible to estimate the free surface velocity.

3.2 Test fluid

The test fluid employed was a solution of carbopol gel 996 with a mass concentration $C_m = 0.125\%$, prepared in accordance with the methodology presented by Minussi and Maciel [30]. Due to its low mass concentration, the gel's density is similar to that of water at ambient conditions, with $\rho = 998$ kg/m^3. Carbopol is the commercial name of polymers vastly employed as thickeners, whose solution might be adjusted to the Herschel–Bulkley rheological model, representative of mud found in tailings dams.

Under simple shear conditions, Eq. (10a) and (b) represent the Herschel–Bulkley rheological model.

$$\dot{\gamma} = 0, \text{if } |\tau| \leq \tau_c \tag{10a}$$

$$\tau = \tau_c + K_n \dot{\gamma}^n, \text{if } |\tau| > \tau_c \tag{10b}$$

In order to establish a reference flow curve for comparing the results of the methodology described in this work, a rheological characterization was carried out by an R/S Brookfield rheometer with controlled shear stress and using CC-45 coaxial cylinders with smooth surface. The measurement protocol consisted of imposing linearly increasing shear stresses from 0 to 70 Pa for 60 points and measuring the shear rates. Then, rheometric data was filtered within the shear rate range observed in the open-channel experiment ($5 < \dot{\gamma} < 80\, s^{-1}$). Four tests were carried to ensure the reproducibility. Figure 4 shows the tests made, the mean flow curve obtained and its 1 standard deviation (1-x_σ) range. The rheometric tests have shown no effects of thixotropy. Table 1 shows the rheological parameters obtained and the respective deviations.

A second reference of rheometric measurement consists in obtaining the material yield stress through the slump test employing a cylindrical mould [33] with the following characteristics: 35.5 mm radius, 94.0 mm height, which gives a volume Vol $= 3.72 \times 10^{-4}$ m^3. In this work, we use the spreading-regime correlation [36] given by Eq. (11):

$$\tau_c = \frac{225 \rho g \text{Vol}^2}{128 \pi^2 R^5}, \tag{11}$$

where R is deformed material's radius after the equilibrium is reached. The reference measurement for τ_c using this technique is also brought in Fig. 4.

3.3 Experimental protocol

Figure 5 shows the experimental protocol. As the protocol demands variation of both channel slope and pump rotation, we defined subscripts for each variable: the subscript i refers to the current channel slope θ and the subscript j

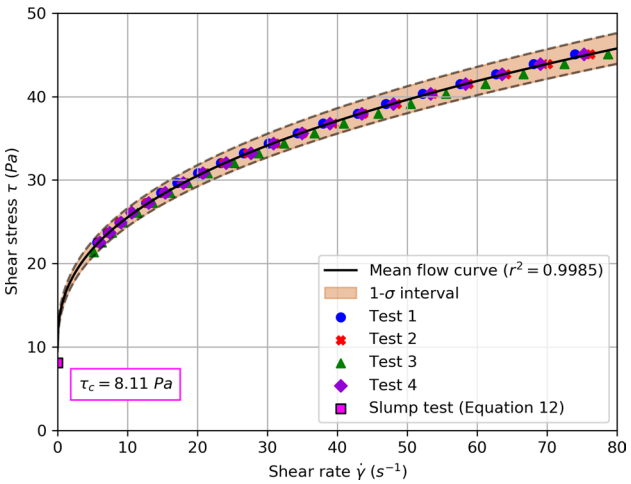

Fig. 4 Flow curve obtained through R/S Rheometer and respective raw data and slump test result for τ_c. Shaded region represents the 1-x_σ interval

Table 1 Rheological parameters obtained through R/S Rheometer fitted by the Herschel–Bulkley model

τ_c (*Pa*)	K_n (Pa.s^n)	n (−)
9.93 ± 0.53	6.21 ± 0.22	0.3994 ± 0.0002

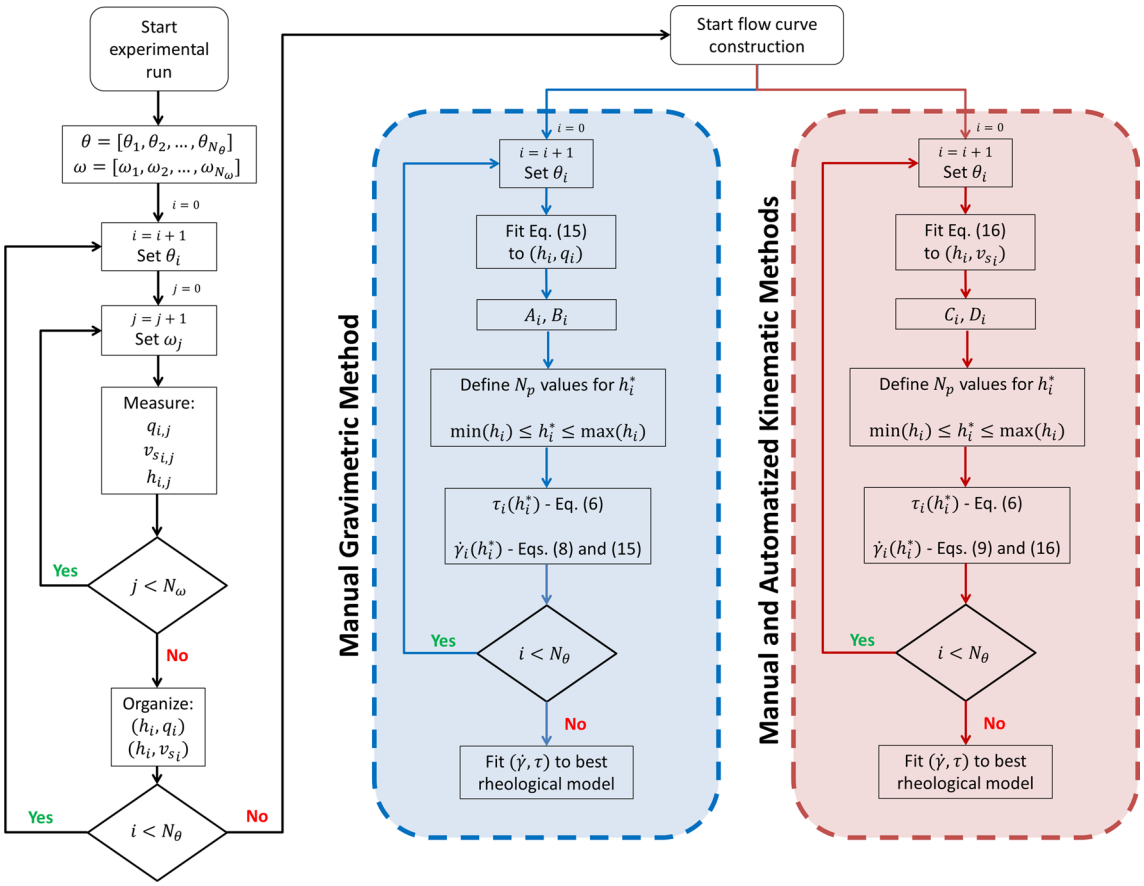

Fig. 5 Experimental protocol for obtaining the flow curve

refers to the current pump rotation ω. For example, $q_{i,j}$ is the specific discharge for the i-th channel slope and the j-th pump rotation. If we evaluate two slopes (e.g., $\theta = 4°$ and 6°), the subscript $i = 1$ refers to $\theta = 4°$ and $i = 2$ to $\theta = 6°$. The same applies to pump rotation and its subscript.

Initially, the channel slope was fixed and the hydraulic pump rotation was altered from 300 rpm to 1000 rpm in steps of 100 rpm, while keeping the suction pipe completely below the free surface height of the reservoir. The number of tests varying pump rotation for each channel is defined as N_ω and the number of channel slopes explored is defined as N_θ. For each combination of slope and rotation, steady state condition was attended when sensors showed no significant local variation of the flow depth (approximately 2 min).

The specific discharge q was measured by collecting the test fluid downstream the channel during a timed period t and measuring the total mass M with a weighing scale. The specific discharge was calculated as Eq. (12) shows, based on the fluid density ρ and the channel width W. Data related to the measures of the specific discharge q are named "Manual Gravimetric Method."

$$q = \frac{M}{\rho t W} \tag{12}$$

The free surface velocity v_s was assessed calculating the time it took for the flow to travel a given distance. Time was taken in two ways: manually by an operator with a chronometer (distance defined as 1 m) and automated by laser barrier sensors (distance defined as 0.5 m). Data related to the experiments where free surface velocity v_s was manually taken by operators are named "Manual Kinematic Method." Data related to the free surface velocity v_s acquired through laser barrier sensors are named "Automatized Kinematic Method."

The normal depth h was measured by the ultrasonic sensor, as discussed in Subsect. 3.1, positioned after 1.5 m from the entrance. Such distance was sufficiently greater than the hydrodynamic entrance length for the experimental runs conducted [1, 37], assuring steady and uniform flow.

After acquiring the necessary data ($q_{i,j}$, $v_{s_{i,j}}$ and $h_{i,j}$), the pump rotation is altered and data is acquired again. After the runs for all pump rotations are explored, channel slope θ was then altered and the flow properties were measured

again for the N_ω rotations as shows Fig. 5. Data are then organized in pairs (h_i, q_i) and (h_i, v_{s_i}) for each slope (i.e., N_θ sets of N_ω pairs of (h, q) and (h, v_s)), where now the subscript j is omitted. With those data, we can start the flow curve construction.

The data are susceptible to uncertainties and should compromise the physical meaning of the shear rates computed through Eqs. (8) and (9). In order to properly apply Eqs. (8) and (9), continuous functions should be fitted to obtain $q(h)$ and $v_s(h)$. Since a vast quantity of time-independent rheological models without viscoelastic effects are available on the literature, a simplifying choice must be made to model $q(h)$ and $v_s(h)$ without the previous knowledge of the rheological behavior of the fluid. Taken, for instance, the fluid-test employed in the present work that was shown to be well-represented by a Herschel–Bulkley rheological model. Based on the theoretical solutions for steady and uniform flow in a rectangular open-channel, one can find the functions from Eqs. (13) and (14) for the specific discharge and the free surface velocity as function of h.

$$q(h) = h\left(\frac{n}{n+1}\right)\left(\frac{\rho g \sin(\theta)}{K_n}\right)^{\frac{1}{n}}\left(\frac{\rho g h \sin(\theta) - \tau_c}{\rho g \sin(\theta)}\right)^{\frac{n+1}{n}} \times \left[1 - \frac{n}{2n+1}\left(\frac{\rho g h \sin(\theta) - \tau_c}{\rho g h \sin(\theta)}\right)\right] \tag{13}$$

$$v_s(h) = \frac{n}{n+1}\left[\frac{\rho g \sin(\theta)}{K_n}\left(h - \frac{\tau_c}{\rho g \sin(\theta)}\right)^{n+1}\right]^{\frac{1}{n}} \tag{14}$$

As a great number of rheological models follows the same topology of the Herschel–Bulkley model regarding the constitutive equation on simple shear (Newtonian, power-law, Carreau, Bingham, Cross, Quemada, K-L model, to name a few), the general behavior of $q(h)$ and $v_s(h)$ can be simplified by using a power-law fitting function as given by Eqs. (15) and (16). For other rheological models, Eqs. (15) and (16) could not be adequate to represent the general behavior of $q(h)$ and $v_s(h)$. Although the choice for a power-law fitting represents a limitation of the methodology, it still may be applied to many materials used in general engineering applications.

$$q(h) = A_i h^{B_i} \tag{15}$$

$$v_s(h) = C_i h^{D_i} \quad , \tag{16}$$

where A_i, B_i, C_i and D_i are fitting parameters for the correspondent θ_i slope.

For each channel slope, an equally spaced set of normal depths h_i^* with an arbitrary number of points N_p is defined. The range of defined values is within the experimental range of h_i ($\min(h_i) \leq h_i^* \leq \max(h_i)$). Then, Eq. (6) is applied to h_i^* to obtain the shear stresses τ_i, and Eqs. (8) and (15) or Eqs. (9) and (16) are used to obtain shear rates $\dot{\gamma}_i$.

Data from each θ_i is then grouped to compose a single data set $(\tau, \dot{\gamma})$ for the flow curve, which may be adjusted to any valid rheological model. The quantity of data points $N_\theta N_p$ employed to calculate the rheological parameters must be sufficient to guarantee independence of the rheological fitting function. For the tests here presented, the number of points employed were greater than 1000, leading to rheological properties variations smaller than 0.1%.

In order to verify and guarantee the laminar flow regime, the Reynolds number Re_H is calculated through Haldenwang's formulation [26] showed by Eq. (17).

$$\mathrm{Re}_H = \frac{8\rho \bar{V}^2}{\tau_c + K_n\left(\frac{2\bar{V}^2}{R_h}\right)}, \tag{17}$$

where $\bar{V}$ and $R_h = hW/(2h + W)$ are the mean velocity and the hydraulic radius, respectively. The Re_H was also used to assure the positioning of sensors past the hydrodynamic entrance length [18, 37].

To control the presence of free surface instabilities, the Froude number Fr was monitored using Eq. (18). Whenever Fr is greater than a minimum value [21, 22], the flow is favorable to the development of free surface instabilities, such as roll waves. This scenario was then avoided and controlled.

$$Fr = \frac{\bar{V}}{\sqrt{gh\cos\theta}} \tag{18}$$

3.4 Experimental uncertainties

Table 2 shows the uncertainties related to the measuring equipment employed in the experiment.

For each composed experimental quantity k (e.g., specific discharge or free surface velocity), uncertainties u_m were accounted for and normalized by the measure m of the

Table 2 Uncertainties related to each measuring equipment of the experiment

Equipment	Uncertainty (u_m)
Weighing scale	0.1 g
Chronometer	0.2 s
Ruler	1 mm
Ultrasonic sensor	0.29 mm
Laser Barrier system	< 0.33%

quantity gauged by each equipment, bringing about the systematic uncertainty $u_{\text{sist},k}$ of the desired quantity k, as shown by Eq. (19).

$$u_{\text{sist},k} = k\sqrt{\sum\left(\frac{u_m}{m}\right)^2} \tag{19}$$

For each experimental run, five measurement repetitions were carried out ($N = 5$). Equation (20) allows estimating the random uncertainties $u_{\text{rand},k}$ based on the number of tests and on the standard deviation s_k of the measurement set.

$$u_{\text{rand},k} = \frac{s_k}{\sqrt{N}} \tag{20}$$

Adopting a confidence interval of 1 standard deviation for $N = 5$, a coverage factor $K = 1.099$ from Student-T Distribution was used. Equation (21) calculates the test's total uncertainty u_k, where $\bar{u}_{\text{sist},k}$ is the average value for the systematic uncertainty of the desired quantity k from the measurement set.

$$u_k = K\sqrt{(u_{\text{rand},k})^2 + (\bar{u}_{\text{sist},k})^2} \tag{21}$$

In order to estimate the experimental uncertainties over the flow curve, we evaluated two limiting scenarios: (1) each measurement of the data set added with the correspondent total uncertainty; and (2) each measurement of the data set subtracted with the correspondent total uncertainty. Then, the two scenarios produce data sets ($(h + u_h) \times (q + u_q)$ and $(h - u_h) \times (v_s - u_{v_s})$) that can be fitted through Eqs. (15) and (16). Both curves are treated as described in Subsect. 3.3 and generate two flow curves using Eqs. (6), (8) and (9), which envelope the mean flow curve. The enveloped areas correspond all possible flow curves that could be obtained within the experimental uncertainties.

4 Results and discussion

The experimental protocol was applied to the data set within the respective ranges brought in Table 3, where dimensionless parameters Re_H and Fr are also brought, calculated by Eqs. (17) and (18), respectively.

Firstly, a qualitative description of the experimental data is performed (Subsect. 4.1), evaluating the model hypothesis and identifying some important aspects of the flow. Secondly, the data fitting and uncertainty analysis are presented in Subsect. 4.2. Finally, the resulting flow curves and the rheological parameters are presented and discussed in Subsect. 4.3. The raw data and other experimental quantities are brought in Appendix 1.

4.1 General aspects and hypothesis validation

A dimensionless analysis of flow parameters (Tables 6, 7, 8, 9, 10, 11, 12, 13, 14, 15, 16) shows that the Reynolds numbers for all experimental tests ranged from 0.14 to 9.89 which verify the laminar flow hypothesis, as the laminar-turbulent transition would start at $\text{Re}_H > 2100$ [7]. The calculated Froude numbers ranged from 0.028 to 0.556 and could indicate the occurrence of roll waves. Even though for some experimental runs (especially those with $\theta > 10°$) showed $\text{Fr} > \text{Fr}_{\text{min}}$, none of the tests conducted presented free surface instabilities evolution. The experimental bench employed was successful to mitigate possible external vibrations. Figures 6 and 7 show Re_H and Fr as function of the dimensionless experimental depth h_E/W, which show how data vary for each slope. A general good behavior of results can be seen, although for some slopes, small discrepancies between kinematic and gravimetric methods are observed.

To verify wide channel hypothesis, we computed the theoretical normal depth h_T according to Eqs. (13) and (14) using the rheometer results, and compared to the experimental normal depth h_E measured through ultrasonic system. Figure 8 presents the behavior of h_T/h_E according to h_E/W.

Tests made with high slopes (e.g., $\theta = 18°$) show small values of h_E/W, presenting a maximum difference of 7% between h_E and h_T ($h_T/h_E = 0.93$). As h_E/W increases, we

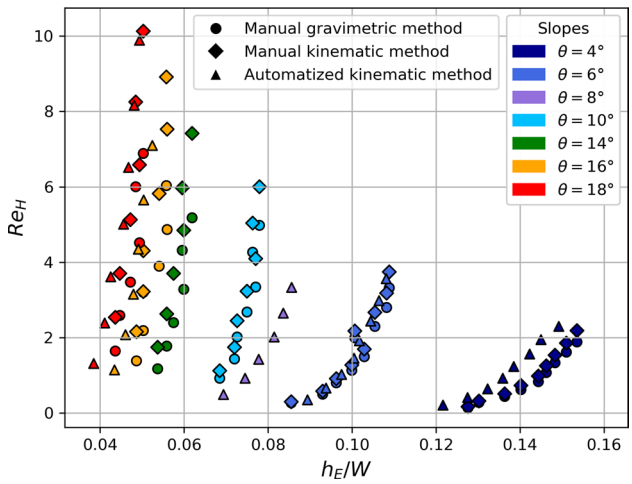

Fig. 6 Evolution of the Reynolds number Re_H in function of dimensionless experimental depth h_E/W

Table 3 Ranges of experimental variables and dimensionless numbers

θ (°)	q (L/s.m)	h (m)	v_s (m/s)	Re_H (−)	Fr (−)
4–18	0.649–3.257	0.0115–0.0460	0.0216–0.2529	0.14–9.89	0.028–0.556

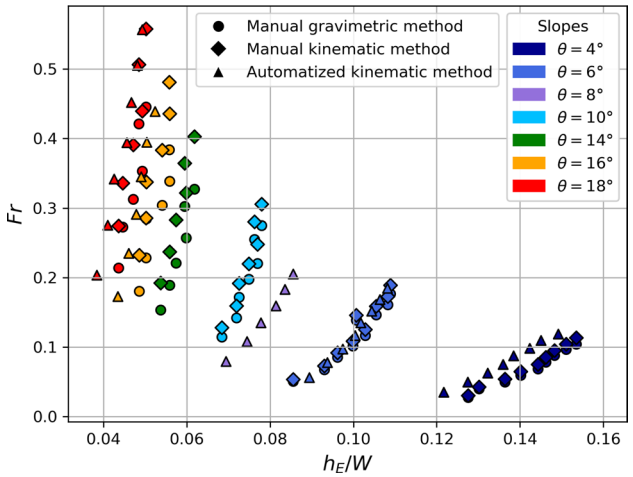

Fig. 7 Evolution of the Froude number Fr in function of dimensionless experimental depth h_E/W

can observe increasingly differences until a maximum difference of 19% for $\theta = 4°$, probably due to effects of lateral edges. In this case, lateral edges contribution to the viscous friction is more prominent, and leads to a deviation of the theoretical solution using the wide channel hypothesis. Even with lateral edges effects, the data presented by Fig. 8 show the adequacy of the experiments regarding the theoretical solutions obtained through the wide channel hypothesis. Based on these observations and on previous works [11], we consider the wide channel hypothesis valid for all the experimental data. Furthermore, the effect of differences between h_T and h_E on the flow curve will be analyzed in Subsect. 4.3.

4.2 Experimental data fitting

The experimental data fitting is crucial to the flow curve obtainment, especially due to the calculation of its shear rates. Therefore, we shall analyze the behavior of q and v_s regarding h and their uncertainties (Tables 6, 7, 8, 9, 10, 11, 12, 13, 14, 15, 16). We first bring the results for the two manual measurement methods employed, and then the automatized one.

Figure 9 shows the experimental data for q using the Manual Gravimetric Method, its absolute uncertainties u_q and h to each fixed value for θ.

As Fig. 9 shows, low values of θ produce high values of h for the same q. To each θ, we can perceive the growth behavior of h produced by the increase of q. This behavior is well described by a power-law fit, as Eq. (15) states, with consistently high values for coefficients of determination r^2 ($r^2 > 0.90$). It is also clear the increasingly value of uncertainties as q increases.

Figure 10 shows the experimental data for v_s, its absolute uncertainties u_{v_s} and h to each θ. For this combination of data, two methods were employed. Firstly, we analyze the data obtained through the Manual Kinematic Method, as shows Fig. 10.

We can observe from Fig. 10 two aspects regarding the flow behavior in relation to θ. First, the higher is θ, the higher are v_s. Second, the variations of free surface velocity are bigger for higher θ values in comparison to lower θ values, demonstrating that higher channel slopes produce higher shear rates when we evaluate the flow curves. Again, the behavior is well described by a power-law fit ($r^2 > 0.90$), as Eq. (16) states. Regarding the uncertainties u_{v_s}, the relative values are lower than u_q and increase as v_s increases.

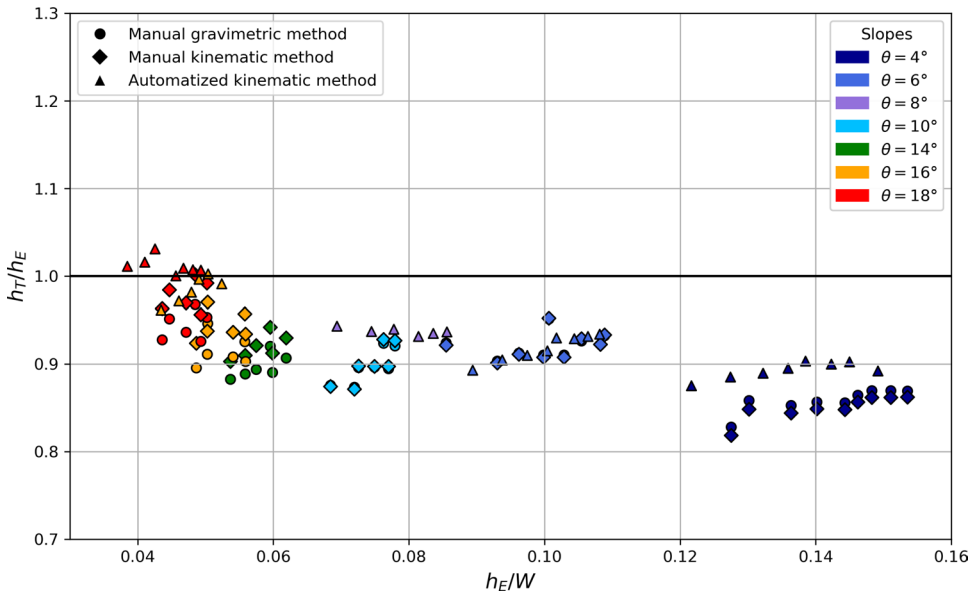

Fig. 8 Comparison between theoretical and experimental normal depth values for all the experimental runs

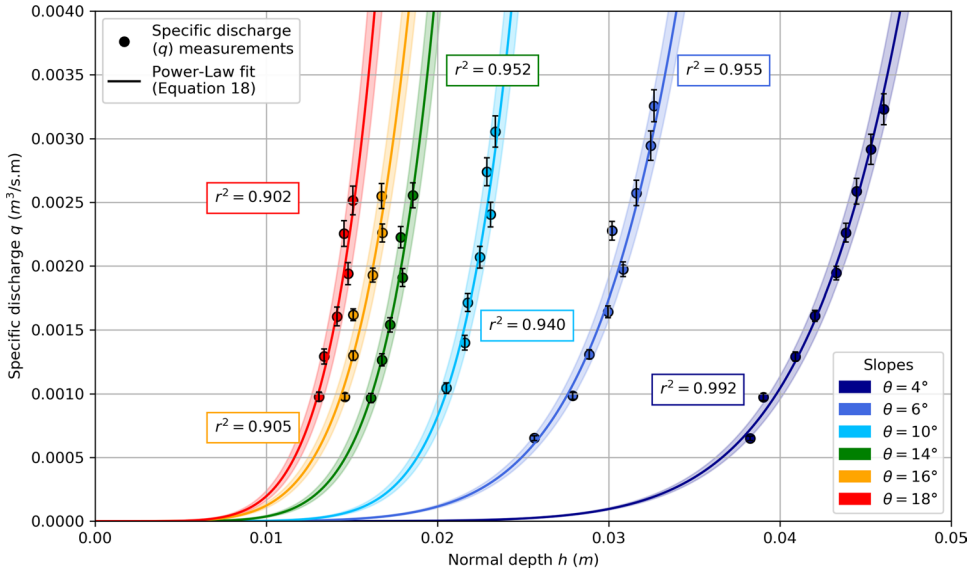

Fig. 9 Specific discharge q (circles) and its uncertainties u_q (vertical bars) as function of the normal depth h. Continuous lines represent the power-law fitting. (Measurements performed through Manual Gravimetric Method)

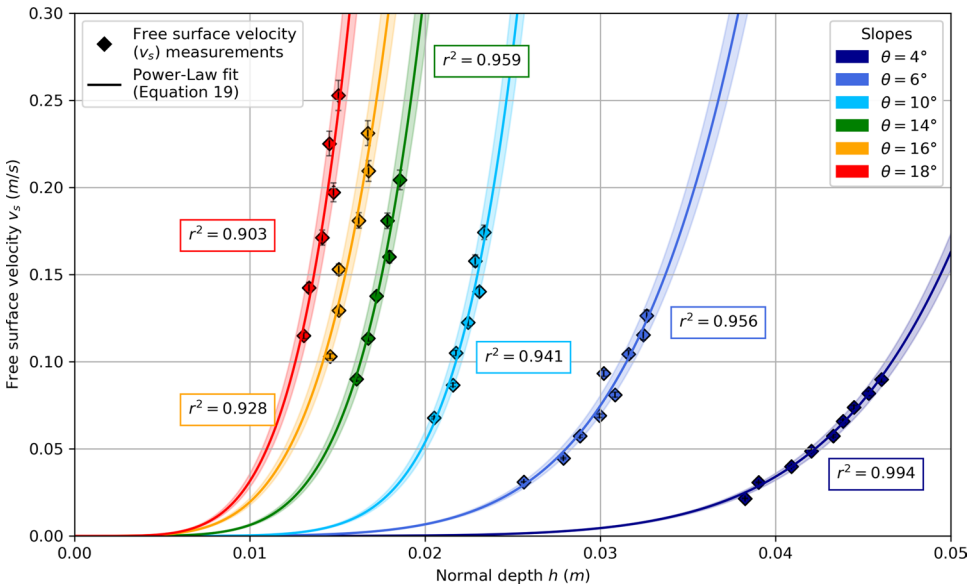

Fig. 10 Free surface velocity v_s (diamond) and its uncertainties u_{v_s} (vertical bars) as function of the normal depth h. Continuous lines represent the power-law fitting. (Measurements performed through Manual Kinematic Method)

Figure 11 shows the experimental data $v_s \times h$ for the automatized kinematic method. It is possible to note the excellent adherence of the power-law fit (Eq. (16)) to the experimental data ($r^2 > 0.98$ for all tests). The uncertainties bars were omitted since they are negligible (< 1.3%), as shown in Tables 12, 13, 14, 15, 16.

To summarize the experimental uncertainties, Fig. 12 shows the relative uncertainties of each target quantity for the three explored methods. We can observe that the free surface velocity uncertainty of the Manual Kinematic Method presents a growing behavior according to the normal depth. It can be observed that the two manual methods produce higher uncertainties (around 5%) than the automatized method (< 0.5%).

4.3 Constructing the flow curve

Beforehand, as brought in Sect. 3.3, we shall highlight the importance of fitting experimental data within the context of calculating $\dot{\gamma}$. If we compute Eqs. (8) and (9) simply as differences between data values (e.g., $\mathrm{d}v_s/\mathrm{d}h \approx (v_{s_{i,j+1}} - v_{s_{i,j}})/(h_{i,j+1} - h_{i,j})$), we would occasionally have incoherent $\dot{\gamma}$ values. To note this issue, one could observe the experimental data from Fig. 10 for $\theta = 10°$, for example. Variations of h due to experimental uncertainties would lead to non-physical $\dot{\gamma}$ values (negative, for example). Thus, the power-law fitting eases and/or allows the calculation of $\dot{\gamma}$ smoothly, and, consequently, the

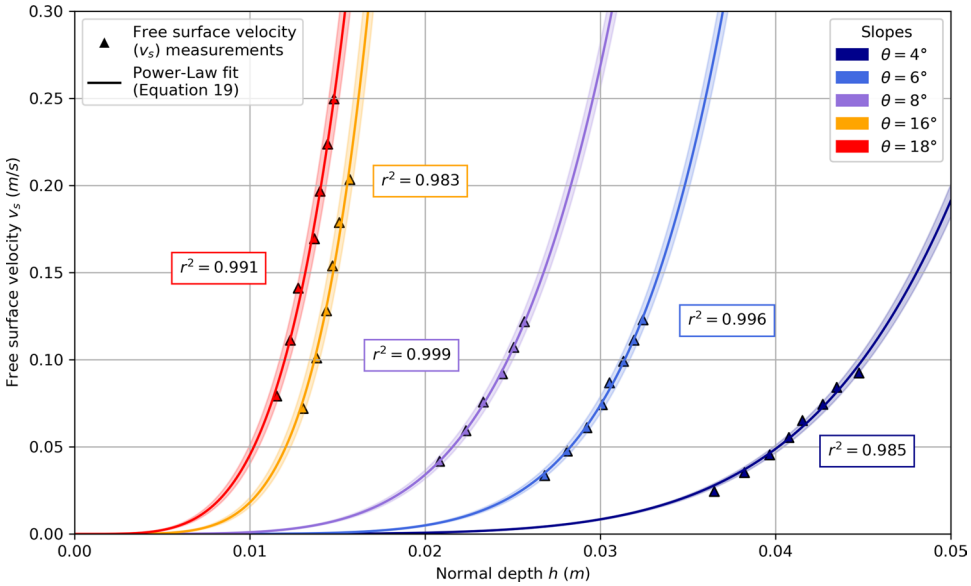

Fig. 11 Free surface velocity v_s (triangle) as function of the normal depth h. Uncertainties were omitted (non-visible). Continuous lines represent the power-law fitting. (Measurements performed through automatized kinematic method)

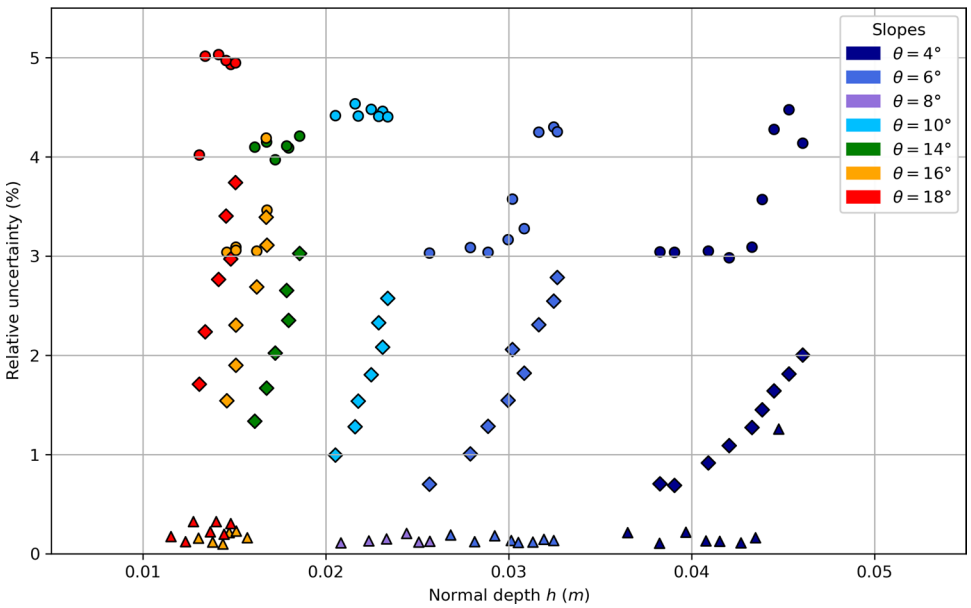

Fig. 12 Relative uncertainty data for Manual gravimetric method (circles), manual kinematic Method (diamond) and automatized kinematic method (triangles)

construction of the flow curve. For practical applications, specially, the lack of precise equipment and control of the flow would cause these issues regarding $\dot{\gamma}$. Therefore, this first data fit of $q(h)$ and/or $v_s(h)$ would allow to better estimate the flow curve, even without proper instruments.

Applying the methodology and considering the Herschel–Bulkley rheological model, the flow curve can be constructed by fitting the Herschel–Bulkley parameters to the points $(\dot{\gamma}, \tau)_i$ for all slopes. Since infinite points could be obtained from the power-law fit for each θ_i, a minimum number of 200 points were gathered to guarantee the independence of the rheological properties ($< 0.1\%$ variation of τ_c, n and K_n to respect the number of points). Moreover, the experimental range of normal depths should limit the employment of the power-law fit to calculating the shear rate data. Then, in the present work, shear rate data was limited according to the method:

- Manual Gravimetric Method: $4.1 < \dot{\gamma} < 65.9\ s^{-1}$;
- Manual kinematic method: $4.6 < \dot{\gamma} < 81.1\ s^{-1}$;
- Automatized kinematic method: $4.7 < \dot{\gamma} < 73.3\ s^{-1}$.

Figure 13 shows the comparison of the reference flow curve obtained by the R/S rheometer (Subsect. 3.2) and the resulting flow curves obtained through the three methods explored by this work. Each of the resulting flow curves is enveloped by the estimated uncertainty area. The result of the slump test, as stated in Subsect. 3.2, is also shown

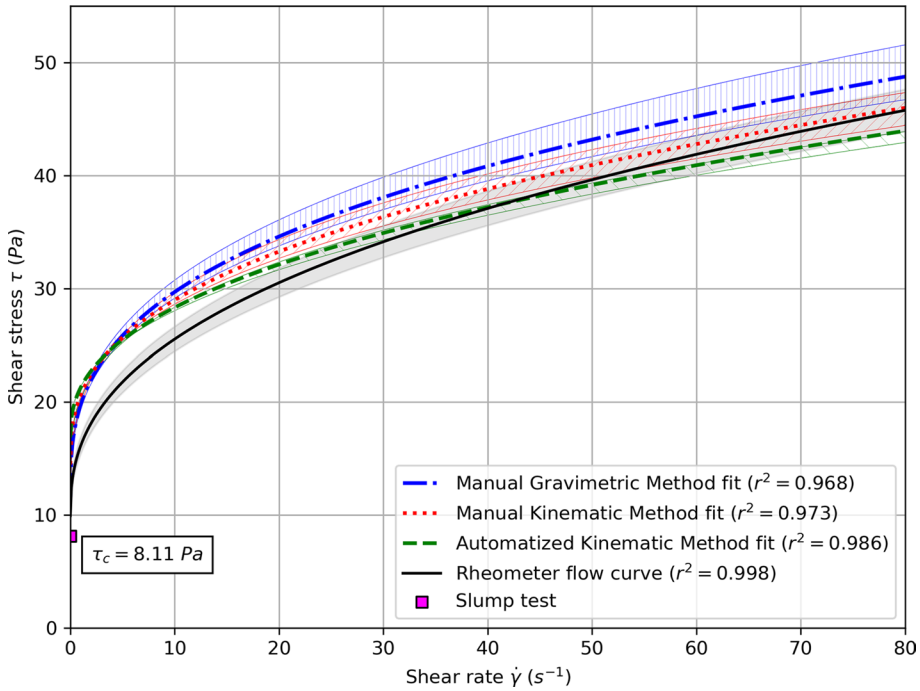

Fig. 13 Comparison of flow curves: reference flow curve obtained through rheometer (continuous line), Manual Gravimetric Method (dash-dot line), Manual Kinematic Method (dotted line), automatized kinematic method (dashed line). The slump test result (square) gives an order of magnitude for the yield stress. Hatched and shaded regions indicate the areas influenced by the experimental uncertainties

in Fig. 13 to establish an order of magnitude for the yield stress.

Figure 13 presents good agreement of data points and the Herschel–Bulkley fit for all methods: $r^2 = 0.968$ for Manual Gravimetric Method, $r^2 = 0.973$ for Manual Kinematic Method and $r^2 = 0.986$ for automatized kinematic method. The good agreement shows the physical consistency of the methodology, producing the expected rheological behavior from the test fluid.

We can note from Fig. 13 that the Manual Gravimetric Method shifts the rheometer flow curve up, presenting discrepancy regarding τ from 15 to 20% for all $\dot{\gamma}$ range. The Kinematic Methods show a similar behavior at $\dot{\gamma} < 25\ s^{-1}$, shifting up the rheometer flow curve. This behavior probably occurs due to possible edge effects for the lowest channel slope, as Fig. 8 shows. Theoretical values for the normal depth h_T are almost always smaller than the experimental values h_E, estimating higher values for τ and shifting the curve up. Such effect is more important when the channel slope is low (e.g., $\theta < 4°$), indicating that the wide channel hypothesis may be compromised. In fact, previous works [11] consider the validity of wide channel hypothesis when $h_E/W < 0.1$, whereas data for $\theta = 4°$ present $0.12 < h_E/W < 0.16$.

As expected, the automatized kinematic method flow curve presents the lowest relative uncertainties regarding $\dot{\gamma}$ (< 5 %). On the other hand, the Manual Methods produced higher relative uncertainties, 18 % and 12 %, respectively. For $\dot{\gamma} > 25\ s^{-1}$, the envelope flow curves of both kinematic methods coincide with the confidence interval of the rheometer flow curve, indicating the adequacy of the methods.

Finally, Table 4 presents the Herschel–Bulkley rheological parameters for experimental runs carried. The errors of each parameter were calculated using the rheometer flow curve as reference.

Even with a limited range of shear rates ($5 < \dot{\gamma} < 80\ s^{-1}$), all methods presented Herschel–Bulkley rheological parameters with the same order of magnitude as the rheometer flow curve parameters, according to Table 4. Values for flow index n showed that all methods are able to properly

Table 4 Herschel–Bulkley rheological parameters for the three explored methods and the rheometer flow curve

	τ_c (Pa)	$\Delta\tau_c$ (%)	K_n (Pa.s^n)	ΔK_n (%)	n (−)	Δn (%)
Rheometer flow curve	9.93 ± 0.53	–	6.21 ± 0.22	–	0.3994 ± 0.0002	–
Manual Gravimetric method	11.58	16.6	8.17	31.6	0.3456	13.5
Manual Kinematic method	14.38	44.8	6.22	0.2	0.3711	7.1
Automatized kinematic method	16.86	69.8	4.42	28.8	0.4136	3.6
Slump test	8.11	18.3	–	–	–	–

Relative errors are based on the Herschel–Bulkley parameters fit for the rheometer flow curve

quantify its value ($\Delta n < 15\%$). We can speculate that producing experimental data for $\dot{\gamma} < 5\ s^{-1}$ would improve the fitted rheological parameters for the inclined channel methods, specially the yield stress.

A speculative analysis can be made based on Fig. 8, considering the differences between experimental and theoretical normal depths (h_E and h_T, respectively) and their effect on the final flow curve. We applied the same procedure described in Subsect. 3.3, using the same configurations, and employed h_T values rather than h_E values to obtain the flow curves. This procedure produced the flow curves shown in Fig. 14. The resulting rheological parameters are shown in Table 5.

The shear rate range remains constrained ($5 < \dot{\gamma} < 80\ s^{-1}$), since the physical characteristics of the flow were not modified and the normal depths were only slightly corrected. We can observe that all methods produce flow curves within the uncertainty range of the rheometer flow curve, and present rheological parameters with errors less than 20%. Based on this correction of the normal depths, the results indicate the deviation of wide channel for some experimental runs.

5 Final remarks

The present work defined and detailed a methodology to employ the flow down an inclined open-channel apparatus to produce the flow curve of a viscoplastic material. The employed mathematical model depends just on variations of specific discharge or free surface velocity and normal depths in steady and uniform conditions.

Regarding the operation of the experimental bench, we observed that manual methods are very sensitive to operator reflexes, whose uncertainties are propagated significantly to the final flow curve. However, the automatized method showed a significant reduction on the uncertainties, eliminating the random sources.

We observed good agreement between experimental and theoretical normal depths, despite the increasingly deviation as the ratio h_E/W increases. The experimental data were well fitted by power-law functions ($r^2 > 0.90$) and ensured the physical coherence considering the theoretical solutions within the shear rate range. Although the power-law fitting should well describe $q(h)$ and $v_s(h)$ for

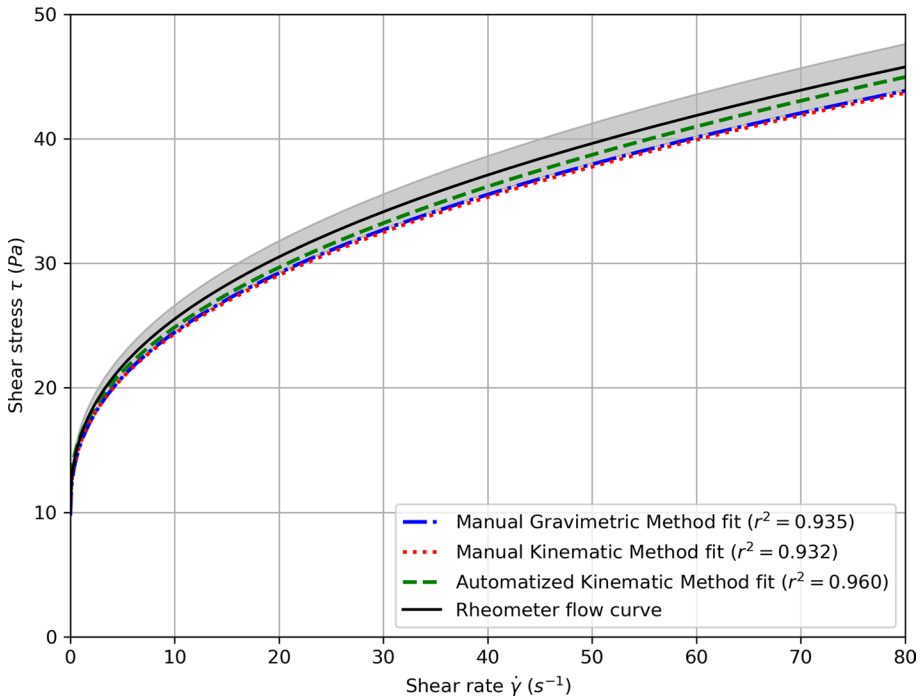

Fig. 14 Comparison between flow curves obtained through the rheometer (continuous line) and those based on the inclined open channel calculated using the theoretical normal depth values (h_T). Shaded region represents the rheometer flow curve 1 standard deviation range

Table 5 Herschel–Bulkley rheological parameters for the three methods calculated with normal depth correction and with the R/S rheometer. Relative errors are based on rheometer flow curve parameters

	τ_c (Pa)	$\Delta\tau_c$ (%)	K_n (Pa.s^n)	ΔK_n (%)	n (−)	Δn (%)
Rheometer flow curve	9.93 ± 0.53	–	6.21 ± 0.22	–	0.3994 ± 0.0002	–
Manual Gravimetric method	9.73	2.01	5.81	6.44	4.039	1.15
Manual Kinematic method	10.22	10.36	5.43	12.56	0.4148	3.91
Automatized kinematic method	11.24	13.21	4.99	19.64	0.4357	9.09
Slump test	8.11	18.3	–	–	–	–

Herschel–Bulkley materials, its simplifications (e.g., Newtonian, power-law and Bingham fluids) and others rheological models with the same constitutive equation topology (e.g., Cross and Carreau), other complex materials could require different fitting functions. However, the hypotheses considered in this work should cover the majority of materials used in general engineering applications.

Using the presented mathematical model and the fitting functions, the obtained flow curves showed relatively good agreement with the Herschel–Bulkley model and were able to present rheological parameters on the same order of magnitude as those estimated by the reference rheometer. All flow curves presented a similar behavior of shifting up regarding the reference flow curve, especially at low shear rates. Correcting the normal depths using the rheometer flow curve parameters, the three methods produced results within the uncertainty region of the reference flow curve, indicating, in fact, the deviation of wide channel hypothesis.

The normal depth corrections and the consequent obtainment of satisfactory flow curves demonstrated that the wide channel hypothesis must be guaranteed; otherwise, the mean flow curve is significantly modified. Although these corrections are biased, since they are calculated based on previously known rheological parameters, the good agreement indicates that the methodology presented in this work can, in fact, produce flow curves with good precision.

Appendix

This Appendix shows the raw data obtained through the methodology described in Sect. 3, presenting measurements of normal depth h, specific discharge q, uncertainties related to specific discharge measurement u_q, free surface velocity v_s and uncertainties related to free surface velocity measurement u_{v_s}. The Reynolds number Re_H, Froude number Fr and minimum Froude number $\mathrm{Fr}_{\min}$ are also calculated as indicated by Subsect. 3.3. The mean velocity $\bar{V}$ for the automatized method was calculated through v_s measurement [20]. Tables 6, 7, 8, 9, 10, 11 present data corresponding to experimental tests made with channel slopes θ of 4, 6, 10,

Table 6 Experimental data measured through Manual Gravimetric Method and Manual Kinematic Method for channel slope $\theta = 4°$

$\theta = 4°$							
h (m)	q (L/s.m)	u_q (%)	v_s (m/s)	u_{v_s} (%)	Re_H	Fr	$\mathrm{Fr}_{\min}$
0.0383	0.649 ± 0.020	3.04	$0.0216 \pm 1.52 \cdot 10^{-4}$	0.71	0.14	0.028	0.182
0.0390	0.974 ± 0.030	3.04	$0.0308 \pm 2.13 \cdot 10^{-4}$	0.69	0.28	0.040	0.184
0.0409	1.291 ± 0.039	3.05	$0.0399 \pm 3.67 \cdot 10^{-4}$	0.92	0.44	0.050	0.190
0.0421	1.612 ± 0.048	2.98	$0.0488 \pm 5.32 \cdot 10^{-4}$	1.09	0.63	0.060	0.192
0.0433	1.944 ± 0.060	3.09	$0.0575 \pm 7.32 \cdot 10^{-4}$	1.27	0.84	0.069	0.196
0.0439	2.261 ± 0.081	3.57	$0.0657 \pm 9.55 \cdot 10^{-4}$	1.45	1.07	0.079	0.197
0.0445	2.586 ± 0.111	4.28	$0.0738 \pm 1.21 \cdot 10^{-3}$	1.64	1.34	0.088	0.198
0.0453	2.915 ± 0.130	4.48	$0.0818 \pm 1.49 \cdot 10^{-3}$	1.81	1.61	0.097	0.200
0.0460	3.230 ± 0.134	4.14	$0.0899 \pm 1.80 \cdot 10^{-3}$	2.01	1.89	0.104	0.202

Table 7 Experimental data measured through manual Gravimetric method and manual Kinematic method for channel slope $\theta = 6°$

$\theta = 6°$							
h (m)	q (L/s.m)	u_q (%)	v_s (m/s)	u_{v_s} (%)	Re_H	Fr	$\mathrm{Fr}_{\min}$
0.0256	0.651 ± 0.020	3.03	$0.0311 \pm 2.19 \cdot 10^{-4}$	0.70	0.27	0.051	0.183
0.0279	0.983 ± 0.030	3.09	$0.0446 \pm 4.50 \cdot 10^{-4}$	1.01	0.50	0.068	0.192
0.0289	1.309 ± 0.039	3.04	$0.0573 \pm 7.38 \cdot 10^{-4}$	1.29	0.80	0.085	0.195
0.0300	1.643 ± 0.052	3.17	$0.0691 \pm 1.07 \cdot 10^{-3}$	1.55	1.13	0.101	0.199
0.0309	1.975 ± 0.065	3.28	$0.0811 \pm 1.48 \cdot 10^{-3}$	1.82	1.50	0.117	0.202
0.0302	2.277 ± 0.081	3.58	$0.0933 \pm 1.92 \cdot 10^{-3}$	2.06	2.00	0.139	0.200
0.0316	2.573 ± 0.109	4.25	$0.1044 \pm 2.41 \cdot 10^{-3}$	2.31	2.30	0.146	0.204
0.0325	2.944 ± 0.127	4.30	$0.1154 \pm 2.94 \cdot 10^{-3}$	2.55	2.80	0.161	0.207
0.0327	3.257 ± 0.139	4.25	$0.1264 \pm 3.52 \cdot 10^{-3}$	2.79	3.32	0.177	0.208

Table 8 Experimental data measured through manual Gravimetric method and manual Kinematic method for channel slope $\theta = 10°$

$\theta = 10°$							
h (m)	q (L/s.m)	u_q (%)	v_s (m/s)	u_{v_s} (%)	Re_H	Fr	$\mathrm{Fr}_{\min}$
0.0205	1.045 ± 0.046	4.42	$0.0678 \pm 6.76 \cdot 10^{-4}$	1.00	0.92	0.114	0.211
0.0216	1.400 ± 0.064	4.54	$0.0867 \pm 1.11 \cdot 10^{-3}$	1.28	1.43	0.142	0.216
0.0218	1.714 ± 0.076	4.41	$0.1050 \pm 1.62 \cdot 10^{-3}$	1.54	2.02	0.172	0.216
0.0224	2.069 ± 0.093	4.48	$0.1226 \pm 2.21 \cdot 10^{-3}$	1.80	2.68	0.198	0.219
0.0231	2.403 ± 0.107	4.46	$0.1402 \pm 2.92 \cdot 10^{-3}$	2.09	3.34	0.220	0.221
0.0229	2.740 ± 0.121	4.41	$0.1580 \pm 3.68 \cdot 10^{-3}$	2.33	4.26	0.254	0.220
0.0234	3.054 ± 0.135	4.41	$0.1742 \pm 4.49 \cdot 10^{-3}$	2.58	4.99	0.275	0.222

Table 9 Experimental data measured through manual Gravimetric method and manual Kinematic method for channel slope $\theta = 14°$

$\theta = 14°$							
h (m)	q (L/s.m)	u_q (%)	v_s (m/s)	u_{v_s} (%)	Re_H	Fr	$\mathrm{Fr}_{\min}$
0.0161	0.966 ± 0.040	4.10	$0.0900 \pm 1.20 \cdot 10^{-3}$	1.34	1.17	0.153	0.219
0.0168	1.265 ± 0.053	4.15	$0.1135 \pm 1.89 \cdot 10^{-3}$	1.67	1.77	0.189	0.222
0.0172	1.541 ± 0.061	3.97	$0.1377 \pm 2.79 \cdot 10^{-3}$	2.03	2.40	0.221	0.224
0.0180	1.909 ± 0.078	4.09	$0.1603 \pm 3.77 \cdot 10^{-3}$	2.35	3.28	0.257	0.227
0.0179	2.223 ± 0.091	4.11	$0.1810 \pm 4.80 \cdot 10^{-3}$	2.66	4.32	0.302	0.227
0.0186	2.553 ± 0.107	4.21	$0.2044 \pm 6.19 \cdot 10^{-3}$	3.03	5.18	0.327	0.229

Table 10 Experimental data measured through manual Gravimetric method and manual Kinematic method for channel slope $\theta = 16°$

$\theta = 16°$							
h (m)	q (L/s.m)	u_q (%)	v_s (m/s)	u_{v_s} (%)	Re_H	Fr	$\mathrm{Fr}_{\min}$
0.0146	0.975 ± 0.030	3.04	$0.1031 \pm 1.59 \cdot 10^{-3}$	1.54	1.39	0.18	0.221
0.0151	1.299 ± 0.040	3.09	$0.1295 \pm 2.46 \cdot 10^{-3}$	1.90	2.19	0.229	0.224
0.0151	1.619 ± 0.049	3.06	$0.1530 \pm 3.53 \cdot 10^{-3}$	2.30	3.20	0.285	0.224
0.0162	1.928 ± 0.059	3.05	$0.1810 \pm 4.87 \cdot 10^{-3}$	2.69	3.90	0.304	0.229
0.0168	2.259 ± 0.078	3.46	$0.2095 \pm 6.52 \cdot 10^{-3}$	3.11	4.87	0.339	0.231
0.0168	2.549 ± 0.107	4.19	$0.2311 \pm 7.85 \cdot 10^{-3}$	3.40	6.03	0.383	0.231

Table 11 Experimental data measured through manual Gravimetric method and manual Kinematic method for channel slope $\theta = 18°$

$\theta = 18°$							
h (m)	q (L/s.m)	u_q (%)	v_s (m/s)	u_{v_s} (%)	Re_H	Fr	$\mathrm{Fr}_{\min}$
0.0131	0.977 ± 0.039	4.02	$0.1150 \pm 1.95 \cdot 10^{-3}$	1.71	1.65	0.214	0.222
0.0134	1.292 ± 0.065	5.02	$0.1425 \pm 3.19 \cdot 10^{-3}$	2.24	2.59	0.273	0.223
0.0141	1.605 ± 0.081	5.03	$0.1712 \pm 4.74 \cdot 10^{-3}$	2.77	3.48	0.313	0.227
0.0148	1.940 ± 0.096	4.93	$0.1972 \pm 5.86 \cdot 10^{-3}$	2.97	4.51	0.353	0.230
0.0145	2.254 ± 0.112	4.97	$0.2252 \pm 7.67 \cdot 10^{-3}$	3.40	6.00	0.421	0.230
0.0151	2.515 ± 0.124	4.95	$0.2529 \pm 9.46 \cdot 10^{-3}$	3.74	6.88	0.446	0.232

Table 12 Experimental data measured through Automatized kinematic method for channel slope $\theta = 4°$

$\theta = 4°$					
h (m)	v_s (m/s)	u_{v_s} (%)	Re_H	Fr	$\mathrm{Fr}_{\min}$
0.0365	$0.0245 \pm 5.23{\cdot}10^{-5}$	0.21	0.21	0.036	0.176
0.0382	$0.0353 \pm 3.86{\cdot}10^{-5}$	0.11	0.41	0.050	0.182
0.0397	$0.0455 \pm 9.89{\cdot}10^{-5}$	0.22	0.64	0.063	0.186
0.0408	$0.0555 \pm 7.41{\cdot}10^{-5}$	0.13	0.92	0.075	0.189
0.0415	$0.0652 \pm 8.21{\cdot}10^{-5}$	0.13	1.23	0.088	0.191
0.0427	$0.0745 \pm 8.24{\cdot}10^{-5}$	0.11	1.56	0.098	0.194
0.0435	$0.0842 \pm 1.37{\cdot}10^{-4}$	0.16	1.95	0.110	0.196
0.0447	$0.0925 \pm 1.01{\cdot}10^{-5}$	1.26	2.30	0.119	0.199

Table 13 Experimental data measured through automatized kinematic method for channel slope $\theta = 6°$

$\theta = 6°$					
h (m)	v_s (m/s)	u_{v_s} (%)	ReH	Fr	$\mathrm{Fr}_{\min}$
0.0268	$0.0335 \pm 6.42{\cdot}10^{-5}$	0.19	0.35	0.056	0.188
0.0281	$0.0477 \pm 5.91{\cdot}10^{-5}$	0.12	0.66	0.078	0.193
0.0292	$0.0611 \pm 1.12{\cdot}10^{-4}$	0.18	1.02	0.097	0.197
0.0301	$0.0744 \pm 1.01{\cdot}10^{-4}$	0.14	1.46	0.117	0.200
0.0305	$0.0869 \pm 9.91{\cdot}10^{-5}$	0.11	1.92	0.135	0.201
0.0313	$0.0992 \pm 1.20{\cdot}10^{-4}$	0.12	2.44	0.152	0.204
0.0319	$0.1113 \pm 1.65{\cdot}10^{-4}$	0.15	2.99	0.169	0.205
0.0324	$0.1230 \pm 1.69{\cdot}10^{-4}$	0.14	3.57	0.185	0.207

Table 14 Experimental data measured through automatized kinematic method for channel slope $\theta = 8°$

$\theta = 8°$					
h (m)	v_s (m/s)	u_{v_s} (%)	Re_H	Fr	$\mathrm{Fr}_{\min}$
0.0208	$0.0417 \pm 4.71{\cdot}10^{-5}$	0.11	0.49	0.079	0.191
0.0223	$0.0593 \pm 7.71{\cdot}10^{-5}$	0.13	0.92	0.108	0.199
0.0233	$0.0758 \pm 1.16{\cdot}10^{-4}$	0.15	1.43	0.135	0.203
0.0244	$0.0920 \pm 1.90{\cdot}10^{-4}$	0.21	2.02	0.159	0.207
0.0251	$0.1071 \pm 1.29{\cdot}10^{-4}$	0.12	2.65	0.183	0.209
0.0257	$0.1220 \pm 1.54{\cdot}10^{-4}$	0.13	3.33	0.206	0.211

Table 15 Experimental data measured through automatized kinematic method for channel slope $\theta = 16°$

$\theta = 16°$					
h (m)	v_s (m/s)	u_{v_s} (%)	Re_H	Fr	$\mathrm{Fr}_{\min}$
0.0130	$0.0720 \pm 1.14{\cdot}10^{-4}$	0.16	1.14	0.173	0.212
0.0138	$0.1012 \pm 1.20{\cdot}10^{-4}$	0.12	2.08	0.235	0.217
0.0144	$0.1282 \pm 1.29{\cdot}10^{-4}$	0.10	3.15	0.291	0.220
0.0147	$0.1540 \pm 3.32{\cdot}10^{-4}$	0.22	4.35	0.345	0.222
0.0151	$0.1789 \pm 4.13{\cdot}10^{-4}$	0.23	5.65	0.395	0.224
0.0157	$0.2035 \pm 3.29{\cdot}10^{-4}$	0.16	7.10	0.439	0.227

Table 16 Experimental data measured through automatized kinematic method for channel slope $\theta = 18°$

$\theta = 18°$					
h (m)	v_s (m/s)	u_{v_s} (%)	Re_H	Fr	$\mathrm{Fr}_{\min}$
0.0115	$0.0793 \pm 1.39{\cdot}10^{-4}$	0.18	1.31	0.204	0.211
0.0123	$0.1114 \pm 1.36{\cdot}10^{-4}$	0.12	2.39	0.275	0.217
0.0128	$0.1411 \pm 4.59{\cdot}10^{-4}$	0.33	3.62	0.342	0.220
0.0137	$0.1694 \pm 3.75{\cdot}10^{-4}$	0.22	5.01	0.394	0.225
0.0140	$0.1969 \pm 6.64{\cdot}10^{-4}$	0.33	6.51	0.452	0.227
0.0144	$0.2238 \pm 4.43{\cdot}10^{-4}$	0.20	8.16	0.506	0.229
0.0148	$0.2498 \pm 7.68{\cdot}10^{-4}$	0.31	9.89	0.556	0.231

14, 16 and 18° using the Manual Gravimetric Method and the Manual Kinematic Method. Tables 12, 13, 14, 15, 16 presents data obtained through the automatized kinematic method with channel slopes θ of 4, 6, 8, 16 and 18°.

Acknowledgements The authors wish to acknowledge FAPESP for financial support under Process 2015/25518-8. Thanks are also given to CAPES for the first author scholarship (88882.433524/2019-01). Finally, the authors thank Doctor Fabiana de Oliveira Ferreira and Associate Professor Doctor Milton Dall'Aglio Sobrinho for their valuable collaboration.

Funding This research was funded by São Paulo Research Foundation (FAPESP) under Process 2015/25518-8 and the Coordenação de Aperfeiçoamento de Pessoal de Nível Superior – Brasil (CAPES) for the first author scholarship (88882.433524/2019-01).

Declarations

Conflict of interest The authors declare that they have no conflict of interest.

References

1. Andersson HI, Shang DY (1998) An extended study of the hydrodynamics of gravity-driven film flow of power-law fluids. Fluid Dyn Res 22(6):345
2. Astarita G, Marrucci G, Palumbo G (1964) Non-newtonian gravity flow along inclined plane surfaces. Ind Eng Chem Fundam 3(4):333–339
3. Baudez JC, Chabot F, Coussot P (2002) Rheological interpretation of the slump test. Appl Rheol 12(3):133–141
4. Bird RB, Dai G, Yarusso BJ (1983) The rheology and flow of viscoplastic materials. Rev Chem Eng 1(1):1–70
5. Boger DV (2013) Rheology of slurries and environmental impacts in the mining industry. Ann Rev Chem Biomol Eng 4:239–257
6. Bonnoit C, Darnige T, Clement E, Lindner A (2010) Inclined plane rheometry of a dense granular suspension. J Rheol 54(1):65–79
7. Burger J, Haldenwang R, Alderman N (2010) Friction factor-reynolds number relationship for laminar flow of non-newtonian fluids in open channels of different cross-sectional shapes. Chem Eng Sci 65(11):3549–3556
8. Carrière S, Jongmans D, Chambon G, Bièvre G, Lanson B, Bertello L, Berti M, Jaboyedoff M, Malet JP, Chambers J (2018) Rheological properties of clayey soils originating from flow-like landslides. Landslides 15(8):1615–1630
9. Chambon G, Ghemmour A, Naaim M (2014) Experimental investigation of viscoplastic free-surface flows in a steady uniform regime. J Fluid Mech 754:332
10. Coleman B, Markovitz H, Noll W, Caswell B (1966) Viscometric flows of non-Newtonian fluids. Springer-Verlag, New York
11. Coussot P (1994) Steady, laminar, flow of concentrated mud suspensions in open channel. J Hydraul Res 32(4):535–559
12. Coussot P, Boyer S (1995) Determination of yield stress fluid behaviour from inclined plane test. Rheol Acta 34(6):534–543
13. Coussot P, Piau JM (1995) A large-scale field coaxial cylinder rheometer for the study of the rheology of natural coarse suspensions. J Rheol 39(1):105–124
14. Coussot P, Proust S, Ancey C (1996) Rheological interpretation of deposits of yield stress fluids. J Non-Newton Fluid Mech 66(1):55–70
15. Coussot P, Laigle D, Arattano M, Deganutti A, Marchi L (1998) Direct determination of rheological characteristics of debris flow. J Hydraul Eng 124(8):865–868
16. Coussot P, Nguyen QD, Huynh H, Bonn D (2002) Avalanche behavior in yield stress fluids. Phys Rev Lett 88(17):175501
17. De Larrard F, Ferraris C, Sedran T (1998) Fresh concrete: a herschel-bulkley material. Mater Struct 31(7):494–498
18. Durst F, Ray S, Ünsal B, Bayoumi O (2005) The development lengths of laminar pipe and channel flows. J Fluids Eng 127(6):1154–1160
19. Fiorot G, Maciel G, Cunha E, Kitano C (2015) Experimental setup for measuring roll waves on laminar open channel flows. Flow Meas Instrum 41:149–157
20. Fiorot GH, de Freitas Maciel G (2019) Free-surface laminar flow of a herschel-bulkley fluid over an inclined porous bed. J Non-Newton Fluid Mech 272:104164
21. Fiorot GH, Ferreira FdO, Dupont P, Maciel GdF (2018) Roll-waves mathematical model as a risk-assessment tool: Case study of acquabona catchment. J Hydraul Eng 144(12):05018009
22. de Freitas Maciel G, de Oliveira Ferreira F, Fiorot GH (2013) Control of instabilities in non-newtonian free surface fluid flows. J Braz Soc Mech Sci Eng 35(3):217–229
23. Gawu SK, Fourie A (2004) Assessment of the modified slump test as a measure of the yield stress of high-density thickened tailings. Can Geotech J 41(1):39–47
24. Ghemmour A, Chambon G, Naaim M (2008) Gravitary free surface flows used as a rheometrical tool: the case of viscoplastic fluids. In: AIP Conference Proceedings, American Institute of Physics 1027:1039–1041
25. Gutierrez L, Pawlik M (2015) Observations on the yielding behaviour of oil sand slurries under vane and slump tests. Can J Chem Eng 93(8):1392–1402
26. Haldenwang R, Slatter P, Chhabra R (2002) Laminar and transitional flow in open channels for non-newtonian fluids. In: Hydrotransport 15: 15th International Conference on the Hydraulic Transport of Solids in Pipes, BHR Group
27. Lavallée Y, Hess KU, Cordonnier B, Bruce Dingwell D (2007) Non-newtonian rheological law for highly crystalline dome lavas. Geology 35(9):843–846
28. Maciel GdF, Santos HKd, Ferreira FdO (2009) Rheological analysis of water clay compositions in order to investigate mudflows developing in canals. J Braz Soc Mech Sci Eng 31(1):64–74
29. Maciel GdF, Ferreira FdO, Cunha E, Fiorot G (2017) Experimental apparatus for roll-wave measurements and comparison with a 1d mathematical model. J Hydraul Eng 143(11):04017046
30. Minussi RB, Maciel GdF (2012) Numerical experimental comparison of dam break flows with non-newtonian fluids. J Braz Soc Mech Sci Eng 34(2):167–178
31. Mizani S, Simms P (2016) Method-dependent variation of yield stress in a thickened gold tailings explained using a structure based viscosity model. Miner Eng 98:40–48
32. Murata J (1984) Flow and deformation of fresh concrete. Mater Constr 17(2):117–129
33. Pashias N, Boger D, Summers J, Glenister D (1996) A fifty cent rheometer for yield stress measurement. J Rheol 40(6):1179–1189
34. Pellegrino AM, Schippa L (2018) A laboratory experience on the effect of grains concentration and coarse sediment on the rheology of natural debris-flows. Environ Earth Sci 77(22):749
35. Piau JM, Debiane K (2005) Consistometers rheometry of power-law viscous fluids. J Non-Newton Fluid Mech 127(2–3):213–224
36. Pierre A, Lanos C, Estellé P (2013) Extension of spread-slump formulae for yield stress evaluation. Appl Rheol 23(9):9. https://doi.org/10.3933/applrheol-23-63849
37. Poole R, Chhabra R (2010) Development length requirements for fully developed laminar pipe flow of yield stress fluids. J Fluids Eng 132(3):034501. https://doi.org/10.1115/1.4001079
38. Roussel N, Coussot P (2005) Fifty-cent rheometer for yield stress measurements: from slump to spreading flow. J Rheol 49(3):705–718
39. Scotto di Santolo A, Pellegrino AM, Evangelista A (2010) Experimental study on the rheological behaviour of debris flow. Natl Hazards Earth Syst Sci 10(12):2507–2514
40. Schatzmann M, Bezzola G, Minor HE, Windhab E, Fischer P (2009) Rheometry for large-particulated fluids: analysis of the ball measuring system and comparison to debris flow rheometry. Rheol Acta 48(7):715–733
41. Schowalter W, Christensen G (1998) Toward a rationalization of the slump test for fresh concrete: comparisons of calculations and experiments. J Rheol 42(4):865–870
42. Zhao C, Zhang M, Zhang T, Wang F, Gao J (2015) Response of roll wave to suspended load and hydraulics of overland flow on steep slope. Catena 133:394–402

Publisher's Note Springer Nature remains neutral with regard to jurisdictional claims in published maps and institutional affiliations.